Journal of Alloys and Compounds 1050 (2026) 185374

Contents lists available at ScienceDirect

Journal of Alloys and Compounds

journal homepage: www.elsevier.com/locate/jalcom

Research article

Strengthening mechanism in Al–Cu–Li alloy processed by friction consolidation followed by high-pressure torsion

Elizabeth Mathew [a,*], Jürgen Markmann [b,c], Chang Yin-Cheng Chan [a], Yulia Ivanisenko [d], Henry Ovri [b], Uceu Fuad Hasan Suhuddin [a], Peter Staron [e], Benjamin Klusemann [a,f]

[a] Institute of Material and Process Design, Helmholtz-Zentrum Hereon, Max–Planck-Straße 1, 21502 Geesthacht, Germany
[b] Institute of Hydrogen Technology, Helmholtz-Zentrum Hereon, Max–Planck-Straße 1, 21502 Geesthacht, Germany
[c] Institute of Materials Physics and Technology, Hamburg University of Technology, Eißendorferstraße 42, 21073 Hamburg, Germany
[d] Institute of Nanotechnology, Karlsruhe Institute of Technology, Hermann-von-Helmholtz-Platz 1, 76344 Eggenstein-Leopoldshafen, Germany
[e] Institute of Materials Physics, Helmholtz-Zentrum Hereon, Max–Planck-Straße 1, 21502 Geesthacht, Germany
[f] Institute for Production Technology and Systems, Leuphana University Lüneburg, Universitätsallee 1, 21335 Lüneburg, Germany

ARTICLE INFO

Dataset link: 10.5281/zenodo.17847594

Keywords:
HPT
FC
SAXS
Al–Cu–Li alloy
Precipitation

ABSTRACT

The primary objective of this study is to explore the precipitation behavior of Al–Cu–Li alloy powder processed through a two-step approach: friction consolidation (FC) followed by high-pressure torsion (HPT). Microstructure analysis by scanning electron microscope shows a refined microstructure after FC, with a further reduction in grain size following HPT. X-ray diffraction analysis confirmed the formation of T_1, T_2, and δ precipitates after FC, which persisted even after HPT. Small-angle X-ray scattering shows a reduction in the volume fraction of larger precipitate particles after HPT, while the smaller grain volume fraction increased. Additionally, the volume fraction of precipitates decreased as a function of strain. To understand the contributions of various mechanisms to an enhanced hardness observed after HPT, a physical model was employed. This study explores how HPT influences dislocation behavior, precipitation, and grain size, highlighting its role in tailoring the microstructure and properties of the friction consolidated Al–Cu–Li alloy.

1. Introduction

Al–Cu–Li alloys are highly suitable for aerospace applications due to their excellent combination of properties, including high strength-to-weight ratio, and strong damage tolerance [1,2]. However, processing of Al–Cu–Li alloys using conventional casting techniques presents significant challenges due to the high reactivity of lithium, which often leads to ingot cracking. Another issue arising from the reactivity of Li is the difficulty in precisely controlling its concentration within the alloy [2]. To overcome these limitations, several alternative fabrication routes that avoid melting, such as severe plastic deformation (SPD) processes using powders, have been explored to improve mechanical properties like strength and ductility [3,4].

Grain refinement and precipitation strengthening significantly enhance the strength of precipitation hardenable aluminum alloys [1,5]. High-pressure torsion (HPT) is a well-established technique for achieving ultra-fine grains (UFG) by introducing a high density of grain boundaries with noticeable misorientations, leading to improved mechanical properties [6–8]. Recent studies have further shown the effectiveness of HPT in Al alloys for achieving significant grain refinement and enhanced hardness [9–12]. Ma et al. [9] showed that solution-treated Al–Cu–Mg alloys subjected to 1–50 turns of HPT exhibited a significant hardness increase after 50 turns, accompanied by substantial grain refinement to an average size of 130–140 nm following subsequent aging at 423 K. Chen et al. [10] showed that HPT processing of an Al–1.0 at.% Mg–0.8 at.% Si–0.2 at.% Mn alloy in the T6 state increased the ultimate tensile strength (UTS) by 81% to 559 MPa while still retaining 14% ductility. After a slight initial drop at 1 turn, further deformation up to 5 turns led to simultaneous increases in ductility, hardness, and UTS. The applied pressure during processing has been shown to influence the alloy's final precipitate structure [13,14]. For example, Qin et al. [15] studied the ageing behavior of Al–Li alloys with the addition of Cu using different deformation methods. Their study revealed that HPT led to the formation of fine precipitates with an average grain size of 120 nm in the Cu containing alloy compared to 210 nm in Al–Li alloys without Cu. This grain refinement attributed to the atomic size and modulus mismatch introduced by Cu, affects the mobility of the dislocations and results

* Corresponding author.
E-mail address: Elizabeth.Mathew@hereon.de (E. Mathew).

https://doi.org/10.1016/j.jallcom.2025.185374
Received 14 October 2025; Received in revised form 18 November 2025; Accepted 29 November 2025
Available online 1 December 2025

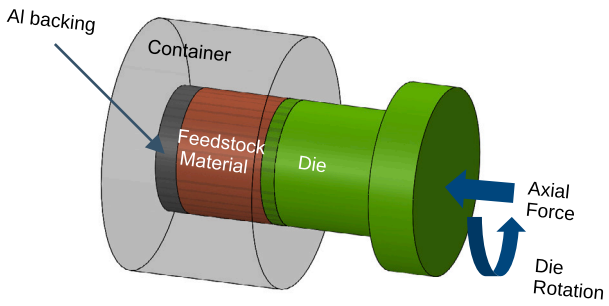

Fig. 1. Schematic illustration of the FC process.

in increased hardness. On the other hand, imposing high strain on the Al–Li alloy resulted in a decrease in hardness. Dong et al. [11] showed that combining HPT with optimized ageing treatments in a 3rd-generation Al–Cu–Li alloy doubled the hardness compared to the T4 state, achieving up to 260 HV, enabled by ultrafine grain refinement, high dislocation density, and strengthening from Cu–Mg clusters distributed in the matrix. However, initial tests within this study (see Appendix A) revealed that Al–Cu–Li powders cannot be adequately processed by HPT alone, as nanosized pores still remain due to the use of powder rather than a standard cast alloy. Furthermore, XRD measurements showed the formation of T_2 precipitates (see Appendix B), which are not the primary strengthening phase in Al–Cu–Li alloys. This finding aligns with thermodynamic calculations (see Appendix D), which indicate that room-temperature HPT conditions favor T_2 formation. Consequently, an additional consolidation step involving temperatures above 150 °C, which enables the formation of the main strengthening T_1 phase, was considered necessary to effectively tailor the mechanical properties of the Al–Cu–Li alloy.

In the present study, an emerging process known as friction consolidation (FC) is adopted as the initial method to consolidate powders prior to HPT. FC is capable of producing consolidated materials at ≈500 °C process temperature with minimal or no defects, along with a more homogeneous microstructure [4,16,17]. FC is a thermo-mechanical process (TMP) in which a rotating die is used to consolidate the feedstock material, such as metal powders or chips, below their melting point [18]. A schematic illustration of the FC process is shown in Fig. 1. During the process, the rotating die applies pressure to the feedstock material, introducing SPD and generating frictional heating. The combination of SPD and elevated temperature results in microstructural refinement through dynamic recrystallization [18]. Catalini et al. [17] demonstrated that FC can yield alloys with low porosity and refined grains from powders feedstock material. Chan et al. [4] showed that in the FCed Al6Cu2Li (wt.%) alloy, which has a composition similar to that studied in this work, T_1 (Al_2CuLi) phase was present as one of the key strengthening phases in Al–Cu–Li alloys.

Several studies have demonstrated the effectiveness of HPT in further improving material performance when used as a second processing step. For instance, in the work of Zubaydi et al. [19], an Al–Si–Cu alloy, processed by laser powder bed fusion (LPBF) and subsequently subjected to HPT, exhibited a higher dislocation density and finer grain size. This combination enhanced the tensile strength and ductility, particularly at higher temperatures and strain rates. Similarly, Stolyarov et al. [20] employed a two-step SPD approach by combining Equal-Channel Angular Pressing (ECAP) and HPT to improve the strength and microhardness of titanium. This improvement was attributed to the increased dislocation density and the development of very fine grains. Recent investigation by Zubaydi et al. [21] on additively manufactured LPBF and HPT-processed Al–Si–Cu alloys reported grain sizes of approximately 66 nm, second-phase particles around 90 nm, and a high dislocation density after room-temperature processing. They showed that HPT enhances both the mechanical performance and microstructural stability of the additively manufactured alloy at room temperature as well as at elevated temperatures, when compared with the as-deposited material and conventional alloy counterparts.

The goal of this study is to understand the microstructural and mechanical changes occurring in FCed Al–Cu–Li powder subjected to subsequent HPT processing. An integrated approach is applied to examine how these advanced powder based processing routes influence the precipitates evolution and grain refinement after each processing stage. The combined use of SAXS and XRD provides insight into deformation-induced fragmentation and dissolution of precipitate phases, as well as the formation of ultra-fine grained microstructures. The experimental results are further correlated with a physical model and measured microhardness to identify the dominant strengthening mechanisms. The findings contribute to advancing the fundamental understanding required to tailor lightweight ultra-fine grained Al–Cu–Li alloys with enhanced mechanical properties.

2. Material and experimental methods

2.1. Material

To prepare the initial powder composition, a glove box (UNIlab Pro, MBraun) with a controlled argon atmosphere was used for both storage and weighing of the material to prevent contamination. The feedstock materials consisted of commercially available powders: AlCu4.5 wt.% (Sindlhauser, particle size below 63 μm), AlLi20 wt.% (American Elements, particle size below 50 μm), and pure Cu (E. Merck KG, particle size below 90 μm). A total of 8 grams of powder was weighed using a high-precision scale (Kern PNS 3000-2) to produce the Al–Cu–Li alloy. The resulting chemical composition (in wt.%) of the prepared Al–Cu–Li alloy was 4.4% Cu, 1.6% Li, and the balance Al.

The 8 g alloy powder was sealed in a container, and thoroughly mixed using a laboratory mixer (MIXOMAT Mini, FUCHS) for 15 min at a rotation speed of 33 rpm. A visual inspection was carried out to ensure homogeneous mixing. Subsequently, the blended powder was compacted inside the container under a load of 40 kN using a manually operated hydraulic 2-column lab press (PW-E, P/O/WEBER) installed within the glove box prior to the FC process.

2.2. Friction consolidation process

FC processing was carried out using the FlexiStir device [22]. To monitor the temperature, a Type K thermocouple was positioned 5.25 mm from the center and 1 mm below the die face. Initially the powder was preheated, a force of 2 kN force was applied for 3.5 s to provide proper contact and prevent torque spikes that could damage the machine. Subsequently, the applied force was set to 12 kN.

The cylindrical 3-scroll die has a diameter of 15 mm, and both the die and the container are made from quenched and tempered AISI 4140 steel. Fig. 2(a) illustrates the die plunge, temperature and force during the FC process at 600 rpm under an axial force of 12kN. During processing, the temperature increased rapidly in the first 30 s and gradually stabilized near 500 °C after approximately 85 s, indicating that the system was approaching thermal equilibrium between frictional heating and heat dissipation. The total processing time was about 96 s. Based on the different die plunge rate, the FC process can be divided into two phases, compaction and consolidation. During the compaction phase, the voids in the powder were largely eliminated; however, the individual powder particles remain separate, and no solid bonds were formed between them. As processing time and temperature increased during the consolidation step, the powder material became softer and more distorted [17]. Once most of the void were removed by the strong compressive force and torque, the intimate contact established between powder particles initiated the mechanical alloying at high strain and temperature [16]. Shearing and frictional heat initially deform and consolidate the upper portion of the material,

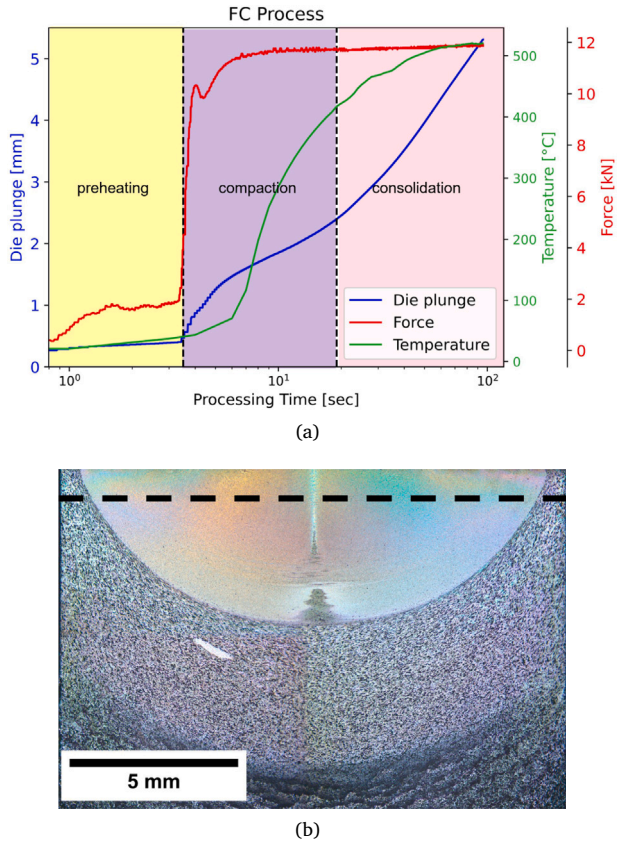

(a)

(b)

Fig. 2. (a) Time-dependent die plunge, process temperature and force during FC; (b) Microstructure of FC sample. The region above the dashed line was further utilized for HPT.

with the consolidation front propagating further away from the die face as processing continued [18]. The resulting billet was a cylinder with a diameter of 15 mm and a height of ≈15 mm. SiC sandpaper was used to remove surface marks left by the die. A diamond wire cutting machine (DIAMOND, WireTec) was used to extract the upper deformed region located above the dashed line in contact with the die, as shown in Fig. 2(b). The extracted sample, 0.8 mm in thickness and 15 mm in diameter, was subsequently utilized for HPT in this study.

The FC parameters of 600 rpm and 12 kN were chosen based on previous studies that optimized the consolidated region to avoid porosity formation during subsequent HPT from powder feedstock (see Appendix E). Lower rotational speeds generally result in insufficient heat input and poor particle bonding, while excessively high rotational speeds may lead to localized overheating or defect formation [23]. Therefore, the adopted parameters represent an appropriate balance between consolidation efficiency and microstructural stability.

2.3. High pressure torsion

Afterwards, the FC sample was subjected to a constrained quasi-hydrostatic HPT process, as shown in Fig. 3. During this process, surface frictional forces cause shear deformation of the disc, enabling deformation to occur under quasi-hydrostatic pressure [6]. The process was conducted at room temperature under a pressure of 5 GPa in a custom-made computer-controlled HPT machine manufactured by W. Klement GmbH (Lang, Austria). The sample was twisted for N = 10 full rotations at a constant rate of 1 rpm. The processing temperature reached ≈40 °C. During HPT, the shear strain γ, along the radius r

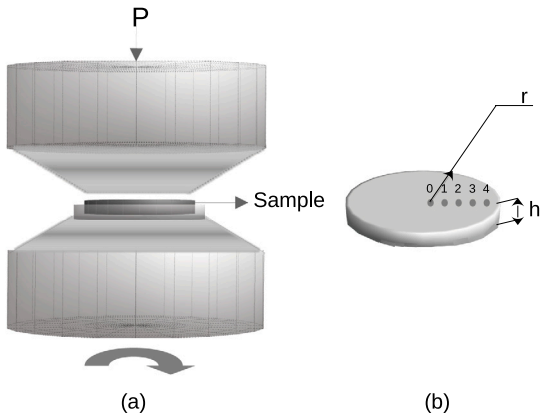

Fig. 3. Schematic illustration of (a) high-pressure torsion (HPT) process showing the direction in which the pressure was applied on the sample and the rotation direction. (b) The processed HPT sample was analyzed along the radius from positions 0 to 4. h represents the height of the sample and r is the radius of the sample.

of the sample and for a constant thickness, h, can be approximated by [6]:

$$\gamma = \frac{2\pi N r}{h}. \quad (1)$$

For aluminum alloys, the HPT conditions of 5 GPa and 10 rotations were chosen from the widely published range of 4–8 GPa and 1–10 turns [6,24,25]. While preserving the integrity of the sample, these parameters guarantee the high shear strain necessary for the creation of ultrafine grains and hardness saturation. Lower pressures (<3 GPa) typically result in heterogeneous grain structures and incomplete deformation. The microstructure and hardness evolve with the number of rotations: As steady-state nanostructure is reached, hardness increases quickly during the first few turns due to dislocation buildup and grain refinement, then gradually saturates beyond 5–10 rotations [6,26].

2.4. Characterization methods

2.4.1. Electron microscopy

High-magnification analysis of the microstructure was performed using an FEI Nova-200 dual-beam SEM operated at 10 kV. An FEI Quanta 650 field emission gun (FEG) SEM equipped with Velocity electron backscattered diffraction (EBSD) detectors was used, and the EBSD data was analyzed using TSL OIM software.

For precipitates observation, high resolution high-angle annular dark-field scanning transmission electron microscopy (HAADF-STEM) was carried out on a lamella of 20 μm × 20 μm extracted through the sample from a region between the center and the edge of the HPT sample. The lamella was extracted from the processed sample with a Ga^+ focused ion beam in the FEI Nova-200 dual beam SEM. The prepared sample was then investigated using Thermo Fisher Talos F200i TEM, operated at 200 kV accelerating voltage.

2.4.2. Phase identification and microstructure analysis using XRD

X-ray powder diffraction (XRD) was employed to characterize the precipitates formed both after FC and FC+HPT processes. XRD measurements were conducted utilizing a Bruker D8 Advance, equipped with a Cu tube operated at 40 kV and 40 mA using CuK_α radiation. The setup included a variable divergence slit of 10 mm spot length, a NiK_β filter, and a position sensitive detector, Bruker LynxEye in fully open configuration.

2.4.3. Small angle X-ray scattering (SAXS) analysis

Small-angle X-ray scattering (SAXS) measurements were performed on a Xenocs Xeuss 3.0 laboratory beam line with a Cu source (wavelength of 0.154 nm) and a Pilatus 3 300K 2D detector. SAXS patterns were background corrected, and normalized to incident photon flux, sample transmission and thickness. The spot size of the X-ray beam was 0.5 × 0.5 mm^2. Since the shear strain within the HPT sample is proportional to the distance from the center of the sample, see Eq. (1), five locations were chosen to be studied by SAXS to examine the impact of shear strain, as shown in Fig. 3(b). All SAXS measurements were carried out within the same week in which the FC+HPT samples were prepared, ensuring minimal microstructural changes prior to analysis.

The detector distance was determined by a calibration measurement of AgBH in the device mounted on the same sample holder. Moreover, due to the stability of the detector vs. the intensity of the primary beam, information about the transmitted intensity was also received. The absolute intensity (I_{abs}) was calculated utilizing:

$$I_{\text{abs}} = \frac{I_{\text{measured}}}{I_{\text{trans}}\left(\frac{S_{\text{pixel}}}{D_{\text{detector}}}\right)^2 T}. \quad (2)$$

Here, $I_{measured}$ is the measured intensity using azimuthal averaging of intensity at each q around the beam center, I_{trans} is the transmitted intensity measured by the device, S_{pixel} is the pixel size of 172 × 172 μm^2, $D_{detector}$ is the detector distance of 1200 mm and T is the measured sample thickness after FC (0.8 ± 0.04 mm) and HPT (0.3 ± 0.02 mm). The thickness was measured using a Vernier caliper, and due to the lateral constraint imposed by the quasi-hydrostatic nature of the constrained HPT process, the thickness reduction during HPT was minimal towards the edge.

The reduced 1D data for the HPT sample included the background contribution from the adhesive tape utilized to hold the sample during SAXS analysis; this background was subtracted accordingly. A model with log-normal size distribution was applied to fit the reduced scattering curves combined with a dilute system with the spherical form factor.

2.4.4. Mechanical testing

Vickers hardness measurements were performed using an EMCO-TEST Durascan 70 G5 with a load of 0.980 N. The measurements were taken along a linear path where the ordinate corresponded to the center of the disc, and the abscissa varied incrementally with a step size of 1.5 mm. This systematic approach allowed for effective mapping of the hardness distribution across the designated segment as a function of strain within the HPT sample.

3. Results and discussion

A rod-shaped sample is obtained after the powder undergoes significant plastic shear deformation during the FC process, resulting in a consolidated sample of the Al–Cu–Li alloy with a refined grain size. Subsequently, a disk-shaped sample cut from the FC rod is subjected to torsional straining under high pressure during HPT processing, which induces further grain refinement. To understand the changes occurring at each process and the mechanisms responsible for the resulting properties, a comprehensive characterization of grain sizes, precipitates morphology and volume fraction, and dislocation density was performed. These aspects are discussed in detail in the following subsections.

3.1. Microstructural characterization

3.1.1. SEM

Fig. 4(a) shows the surface of the FC sample. A distinct pattern is visible on the top, originating from the 3-scroll die shape. The inset map confirms that the powder was fully consolidated with no pores observable in the FC processed sample. However, some Cu particles remain. Fig. 4(b) illustrates the inverse pole figure (IPF) map, highlighting the grain structure and orientation distribution, while Fig. 4(c) summarizes the grain size distribution, with an average grain size of 2.7 μm. During friction consolidation, dynamic recovery creates new subgrain boundaries as a result of the substantial deformation. Frictional heating and the severe plastic strain further reduce the subgrain size. Eventually, continuous dynamic recrystallization generates equiaxed grains, leading to effective grain refinement [27]. It is well documented that HPT results in UFG [6,28], therefore additional TEM analysis was carried out to analyze the grain size of the HPT sample.

3.1.2. TEM

As shown in Fig. 5(a), dislocations are visible within the grains, and the microstructure is very fine grained after FC+HPT. It is known that the high dislocation density introduced by HPT at room temperature results in significant local strain differences, which are evident in an TEM image [29]. Moreover, no precipitates were observed after HPT. Murayaa et al. [30] claim that after HPT, small particles apparently dissolved into the matrix due to the significant release of surface free energy from the fragmented UFG.

Fig. 5(b) show an average grain size of around 52 ± 37 nm after FC+HPT. This grain size falls within the range for the Al–4%Cu HPT powder consolidation reported by Hasse et al. [31], who found that grain size drops from ≈110 nm at 1 rotation to ≈55 nm and 48 nm for 30 and 100 rotation, respectively. Their study also proved that the coherent domain size decreases drastically with increasing the number of HPT rotations from one to ten, after which it remains constant. The FC process results in a grain-size gradient, as the region in contact with the die experiences higher strain and temperature, leading to finer dynamically recrystallized grains near the interface [32]. After subsequent HPT processing, ultrafine grains are formed throughout the sample, producing a grain-size gradient that extends from the finer grains near the die interface to slightly coarser grains further away, as the measurement spans through the sample thickness. Moreover, the ring-shaped SAED patterns in the upper right corner of Fig. 5 with the dispersed diffraction rings further confirm the grain refinement after HPT. However, the complex diffraction contrast makes it difficult to distinguish precipitate details. Therefore, XRD was performed to obtain complementary information on the precipitates formed after FC and FC + HPT. Furthermore, the SAXS measurements performed in transmission mode provide complementary information averaged through the sample thickness.

3.2. XRD

Fig. 6 illustrates the expected shapes of the precipitates, an important information which is essential for calculating the size distribution in SAXS. T_1 phase is a strengthening phase that nucleates on dislocations [1]. It appears as platelets within the Al matrix and exhibits a hexagonal structure [5]. Various crystal structures of T_1 have been proposed in literature [33,34]; however, the structure reported by Van Samaleen et al. [33] is widely accepted since later HAADF-STEM studies confirmed its validity [34]. Therefore, this structure was adopted for identifying T_1 in the present work. T_2 precipitates are elliptically shaped-like and commonly located at grain boundaries, showing a quasicrystal isochedral structure [35]. δ precipitates are also spherical. Both T_2 and δ are responsible for controlling the toughness of the material [1].

The XRD diffractogram in Fig. 7 for the friction consolidated sample shows the presence of Al (α phase), δ, T_2 and T_1 precipitates. These phases were retained after HPT. Another notable observation is a step-like feature, highlighted by a red circle in the inset image, which appears in the Al (111) peak. This feature is a typical indication of the X-ray absorption edge of the Ni filter for the K_β peaks, which are

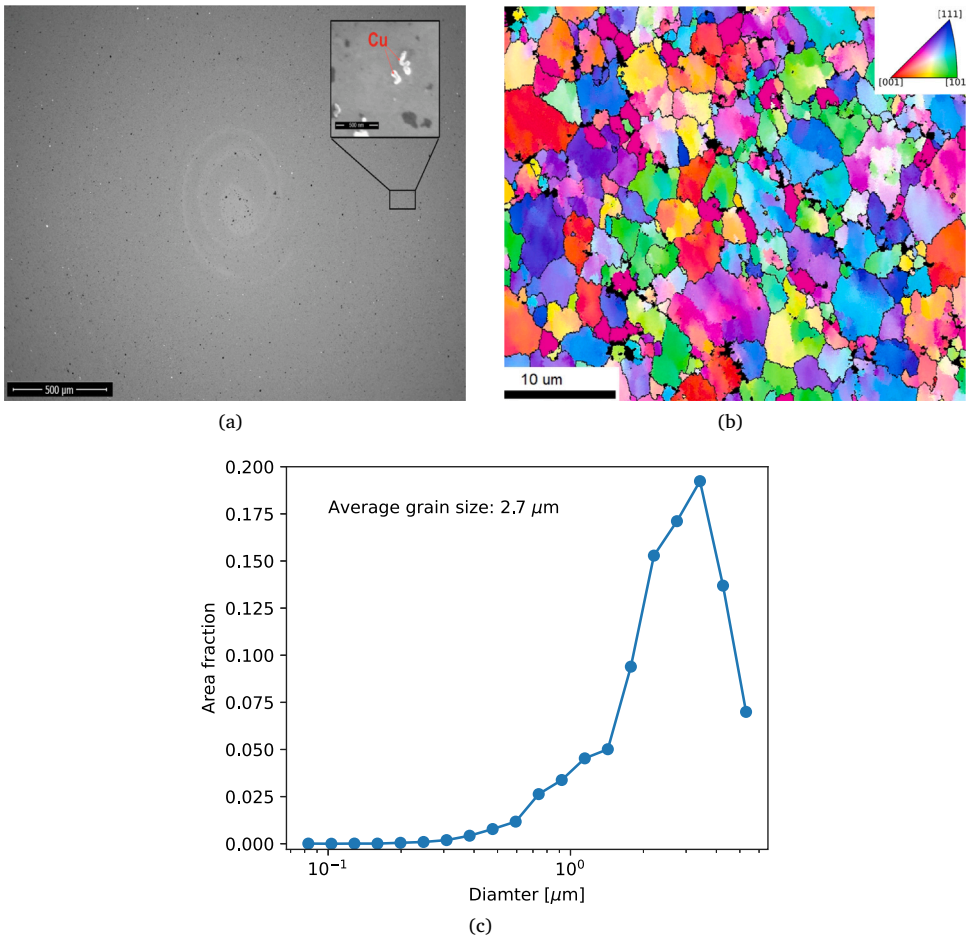

Fig. 4. SEM characterization: (a) micrograph showing surface morphology of FC sample, inset map confirms no pores with Cu particles; (b) Inverse Pole Figure (IPF) map depicting crystallographic grain orientation of FC sample; (c) Average grain size distribution of FC sample determined from the IPF analysis.

Table 1
Coherent domain size, microstrain, dislocation density of α phase obtained using the XRD results for FC and FC+HPT process.

Process	Coherent domain size [nm]	Microstrain [%]	Dislocation density $\times 10^{10}$ [cm^{-2}]
FC	88.09	0.02	0.09
FC+HPT	47.12	0.14	4.34

visible only for very intensive peaks when displayed on a logarithmic scale. Moreover, the intensities of the Al peaks decrease after HPT. This indicates that HPT alters the crystallographic texture of the alloy. Another notable aspect is the peak broadening observed for the Al (111) after HPT, which is attributed to the decrease in coherent domain size and the increase in strain [36]. Another peak of Al (111) appears at $2\theta = 34.2^{o}$ as marked by the arrow in Fig. 7, which is caused by the K_{β} Cu X-ray.

The reflection from the diffraction results exhibit $K_{\alpha 1}$ and $K_{\alpha 2}$ doublets, which were fitted using the Pearson VII doublet function with open-source Python libraries. Instrumental broadening was calculated from the full-width half maxima (FWHM) of the diffractograms using a NIST 660b LaB_6 standard. The Cagliotti function was fitted to the FWHM of LaB_6 standard. The final broadening was calculated by subtracting the instrumental FWHM.

The microstrain (e) was calculated utilizing the following formulation [37]:

$$\frac{(\delta q)^2}{q^2} = \frac{8\pi K}{3D}\frac{\delta q}{q^2} + 4e^2, \tag{3}$$

where q denotes the magnitude of the scattering vector, defined as $q = 4\pi \sin(2\theta/2)/\lambda$, with λ and 2θ representing the wavelength and the scattering angle, respectively. The variation of q, denoted as δq, is determined by the peak width $\delta(2\theta)$ and is given by $\delta q = 2\pi\lambda^{-1}\cos(2\theta/2)\,\delta(2\theta)$. In this expression, K is the Scherrer constant (0.893), and D is the grain size of the coherently scattering particle.

The strain broadening obtained from the diffractograms was used to approximate the dislocation density (ρ) according to [38]:

$$\rho = \frac{\kappa e^2}{F b^2}. \tag{4}$$

For face-centered cubic materials, $\kappa = 16.1$, F is the interaction factor assumed as 1 here and $b = 2.85 \times 10^{-8}$ cm is the Burgers vector length, where $\vec{b} = 1/2 < 110 >$ in aluminum [38].

The slope and the intercept were used to compute the coherent domain size and microstrain in accordance with Eq. (3), while the dislocation density ρ was estimated by Eq. (4). The computed dislocation density, microstrain, and coherent domain size are summarized in Table 1. It is important to note that only the position and width of the Al peaks were considered for the dislocation density calculation; therefore, the microstrain values and calculated crystallite sizes are those of the Al phase.

Compared to the FC sample, the FC+HPT sample showed a drop in coherent domain size and an increase in both microstrain and dislocation density. The significant increase in dislocation density after HPT is attributed to the severe strain introduced during HPT processing. Furthermore, HPT generates less frictional heat than FC due to its lower rotational speed. As a result, the dislocations created during

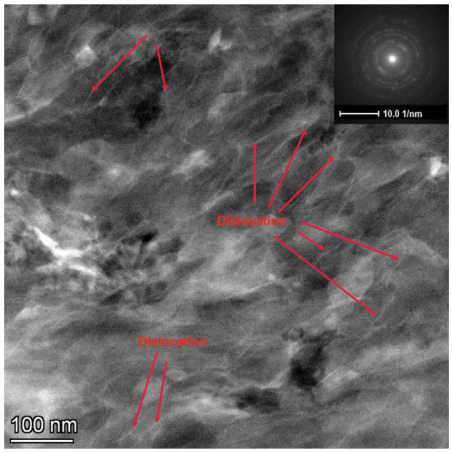

(a)

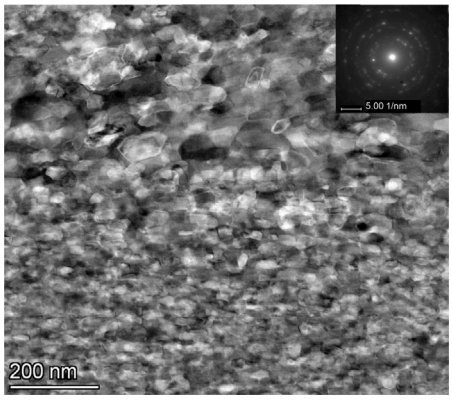

(b)

Fig. 5. TEM microstructural characterization of position 3 of HPT sample, see Fig. 3(b), (a) HAADF image at a higher magnification; (b) DF2 image showing ultra-fine grains.

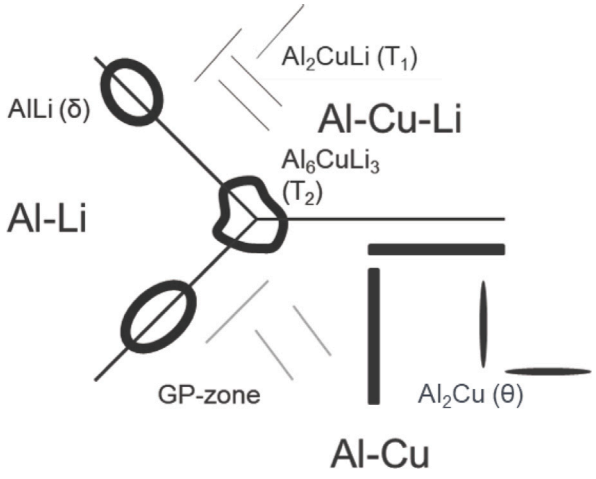

Fig. 6. Expected shape of the precipitate for Al–Cu–Li alloys with Li < 2% adapted from the literature [1,5].

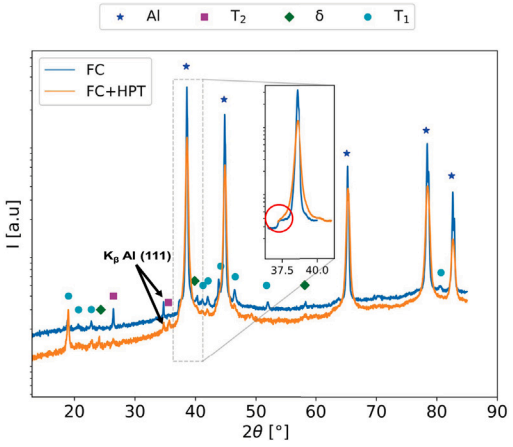

Fig. 7. XRD diffractograms of FC and FC+HPT processed Al–Cu–Li alloy.

severe deformation are retained, and recrystallization and recovery are suppressed [29].

The formation of T1 precipitates in Al–Cu–Li alloys with similar composition after FC has already been reported [4]. It is worth noting that despite the XRD peaks of particles still present in the XRD diffractogram after HPT, particles could not be observed via TEM. This is most likely due to the fragmentated nature of fine precipitates, which exhibit low contrast against the matrix, particularly for the coherent and semi-coherent precipitates. For such fine precipitates, the strain-field contrast is likely the dominant imaging mechanism [39]. Additionally, the high dislocation density and the refined grain sizes introduced complex strain fields, further complicating direct observation of precipitates. Consequently, direct visualization of precipitates in HPT studies is rarely reported in the literature [11,40,41]. Therefore, to obtain a global understanding of the precipitate size and volume fraction, SAXS was utilized.

3.3. SAXS

The SAXS signal was recorded from the center to the periphery of the FC+HPT sample to study the effect of strain. The SAXS 1D integration as shown in Fig. 8(a) confirms a reduction in intensity with increasing strain, suggesting that strain leads to the dissolution of precipitates. The dissolution process of precipitates due to shear during HPT has been reported by several authors [30,42,43].

Fig. 8(b) shows the volume fraction of T_1 precipitates as a function of size. The 1D data were fitted using a bimodal log-normal distribution to capture the effects of shear deformation. The larger population corresponds to the relatively coarse precipitates retained after FC and HPT, which experienced limited deformation, whereas the smaller population arises from recrystallized precipitates formed during FC and from fragmented precipitates generated during HPT (see Appendix C). Several assumptions were made during the fitting process:

a. Particle Geometry Approximation: The plate-like precipitates were assumed to scatter isotropically, modeled as spherical particles. This simplification was necessary because the obtained 2D SAXS signal was isotropic, even though it might not fully represent the true geometry of plate-like structures. Moreover, previous studies [44] have shown that for plate-like systems, SAXS fits using sphere and disc form factors yield nearly identical average sizes and volume fractions, with only the number density being significantly affected by the chosen model. In addition, T_2 (Al_6CuLi_3) and δ (AlLi) precipitates, which are roughly spherical, coexist with T_1 plate-like precipitates. Since the lateral dimensions of T_1 and the radii of T_2 and δ are comparable, distinguishing between these two geometries was not feasible. Therefore, the derived

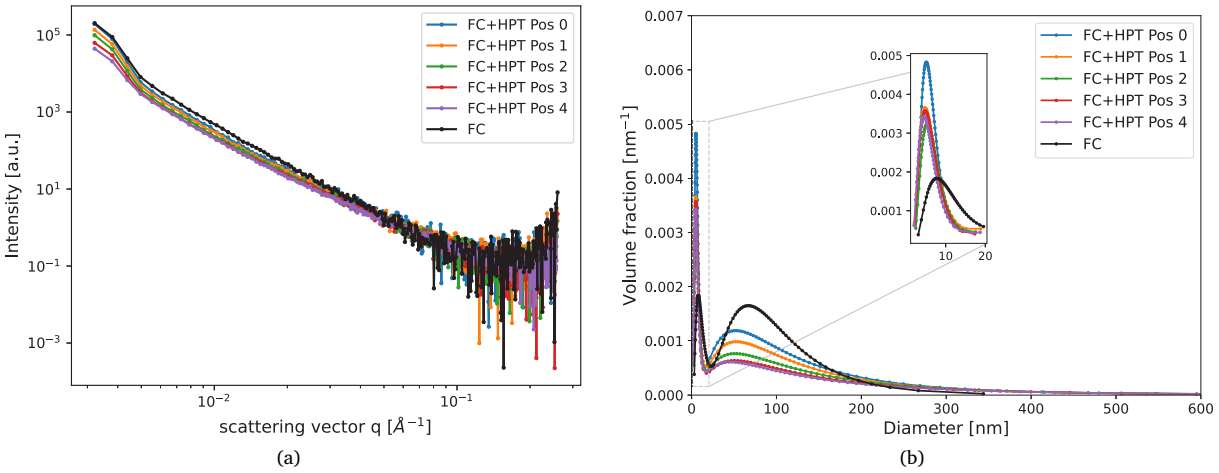

Fig. 8. SAXS analysis of FC and FC+HPT: (a) 1D reduced plot obtained after isotropic azimuthal averaging of intensity at each q performed around the beam center coordinates; (b) precipitate size distribution obtained after bimodal log-normal fitting. The SAXS signals were recorded for every point from position 0 to 4 as shown in Fig. 3(b).

radius represents the lateral dimension of T_1 and the radius of T_2 and δ.

b. Scatterer Interaction: Minimal interaction between scatterers was assumed, which holds true for a dilute system, where precipitates are well separated within the matrix.

c. Electronic Contrast: A constant electronic contrast was used for bimodal log-normal distributions, justified by the observation that larger particles fragment into smaller ones after HPT.

As shown in Fig. 8(b), two distinct distributions were observed for both the FC and the FC+HPT samples. The fitting suggests that the applied strain causes partial dissolution of precipitates. The mean diameter of T_1 precipitates for the FC sample is 95 ± 65 nm and approximately 98 ± 56 nm for FC+HPT. Chan et al. [4] reported a slightly larger average T1 diameter of 121 ± 37 mm for an FC AlCu6Li2 (wt.%) alloy of slightly different composition. The average diameter of the T_2 precipitate is 140 ± 50 nm [45].

At very high strains, the dominance of smaller precipitates due to fragmentation, combined with residual larger precipitates, results in an increase in the volume of the smaller distribution after HPT, see Fig. 8(b). This behavior reflects the fragmentation of T_1 and T_2 precipitates caused by the intense shear deformation and strain localization during HPT. The resulting high dislocation density and ultrafine grain structure enhance solute mobility and interfacial energy, promoting the dissolution of smaller precipitates and limiting their re-precipitation in the absence of a subsequent aging treatment [11,46]. Consequently, the mean size of the first distribution decreases with strain: from 10 ± 4 nm in the FC sample to 6 nm in the FC+HPT sample, and further reducing slightly to 5 ± 2 nm with increasing shear strain.

3.4. Discussion on the strengthening mechanisms based on theoretical model

The Vickers microhardness maps of the FC and FC+HPT samples as a function of distance from the center are displayed in Fig. 9. The mean hardness after FC is 118 HV while for FC+HPT it increased to 242 HV. The relatively high hardness in the FC+HPT sample can be attributed to the ultra-fine grains and the large amount of dislocations [29]. Another notable aspect of the FC+HPT sample is that, despite the strain gradient, the hardness is nearly constant aside from a small reduction at the center. This behavior is expected for samples processed with 10 HPT rotations [6]. As it is generally accepted that hardness and yield strength are proportional and both measure a material's resistance to plastic deformation, the yield strength can be approximated as [47,48]:

$$\sigma_y^{exp} = C\ HV_{0.1}, \tag{5}$$

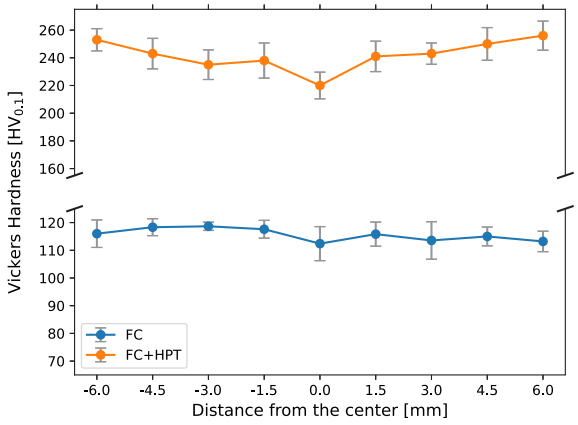

Fig. 9. Hardness distribution of FC and FC+HPT.

where σ_y^{exp} is the yield strength (unit MPa), C is a constant, often taken equal to 3 for most metals [11,49] including ultra-fine grained Al alloys [50,51], and $HV_{0.1}$ is the measured Vickers hardness value.

The contribution from the various strengthening mechanisms is taken into consideration to comprehend the mechanisms governing the strength of Al–Cu–Li alloy. According to several researchers [52–55], the strength in aluminum alloys can be theoretically described by

$$\sigma_y = \sigma_i + \sigma_{gb} + \sigma_d + \sigma_{ss} + \sigma_p, \tag{6}$$

where, σ_i represents intrinsic yield strength due to lattice friction, σ_{gb} grain boundary strengthening, σ_d dislocation strengthening, σ_{ss} solid solution strengthening, and σ_p represents the particle strengthening, all contributing to the yield strength σ_y. The increase in yield strength due to short-range order is not considered, since Mg is absent in the current Al–Cu–Li alloy to form Cu-Mg clusters. Ivanov et al. [56] noted that hardness increase due to short-range ordering occurs only when Mg is present.

The strength of annealed aluminum, σ_i, is extremely low (about 20 MPa for high purity Al 99.99% [57]). In the following section, the predicted contributions of the remaining strengthening mechanisms are presented for the UFG Al–Cu–Li alloy after FC and FC+HPT.

Table 2
Parameters used in calculating strengthening mechanisms.

Mechanism	Parameters	Symbol	Values	References
	Taylor factor	M	2.6	[11,48,52]
	Burger vector	b	0.285 nm	[38,47]
	Shear modulus of Al	G	27 GPa	[47,48]
Grain boundary strengthening	Hall-Petch constant	k_{hp}	0.08 MPa/m^2	[59,60]
	Grain size	d	FC: 2.7 μm FC+HPT: 52 nm	this work
Dislocation strengthening	Constant	α_1	0.3	[48]
	Dislocation density	ρ	FC: 0.09 x 10^{14}m^{-2} FC+HPT: 4.34 x 10^{14} m^{-2}	this work
Solid solution strengthening	Strengthening factor of Cu	k_{Cu}	10 MPa/at.% Cu	[49,54]
	Strengthening factor of Li	k_{Li}	6 MPa/at.% Li	[49,54]
	Concentration of Cu	c_{Cu}	1.83 at.%	See Section 3.4.3
	Concentration of Li	c_{Li}	6.11 at.%	
Particle strengthening	Thickness of T_1	t_p	1.4 nm	[1]
	Diameter of T_1	d_p	FC: 95 nm FC+HPT: 98 nm	this work
	Volume fraction of T_1	f_p	FC: 1.3% FC+HPT: 0.9%	this work

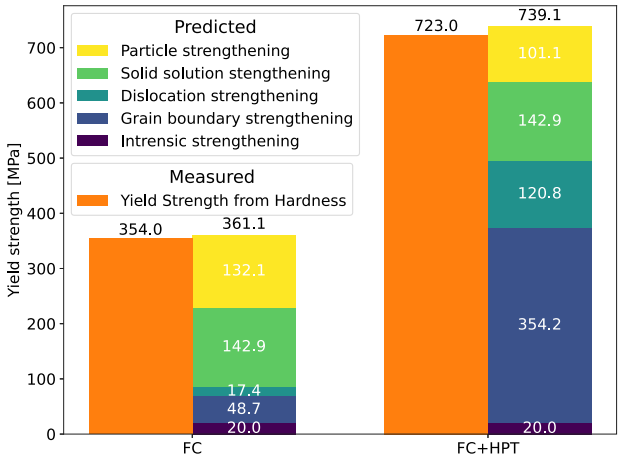

Fig. 10. Comparison of yield strength measured by Micro-Hardness tests with yield strength estimated from the Strengthening Model. All values are in MPa.

3.4.1. Grain boundary strengthening

The Hall-Petch relationship is used to determine the yield strength resulting from grain boundary strengthening [58]:

$$\sigma_{gb} = k_{hp} d^{-n}. \tag{7}$$

The Hall-Petch constant, k_{hp} = 0.08 MPa m$^{-1/2}$, is reported for Al–4%Cu alloy [59], which closely resembles the alloy composition used in this study. Here, d represents the grain size that was calculated from the microstructure. For coarse-grained metals, the exponent n = 1/2 is typically employed to evaluate strengthening behaviors using the conventional Hall-Petch relation. Grain size was determined from SEM images for FC samples and TEM images for FC+HPT samples, see Table 2.

3.4.2. Dislocation strengthening

The motion of interacting dislocations is impeded. Consequently, an increase in dislocation density results in a rise in hardness [53,54]:

$$\sigma_d = M \alpha_1 G b \sqrt{\rho}, \tag{8}$$

where M represents the Taylor factor, α_1 is a constant and G is the shear modulus of Al. The dislocation density is obtained via Eq. (4), see results in Table 2.

3.4.3. Solid solution strengthening

The concentration of solute atoms dissolved in the Al matrix determines the strength of the solid solution as [47]:

$$\sigma_{ss} = M \sum k_j c_j^{n'}, \tag{9}$$

where k_j signifies the strengthening factor for individual alloying elements and c_j indicates the concentrations of the alloying elements in solid solution, and n' is a constant taken as 1. These factors are obtained from literature and c_j is calculated based on the alloy composition in at.% [11]. In the present work, the primary contribution arises from Li due to its higher concentration.

3.4.4. Particle strengthening

The primary strengthening precipitate in Al–Cu–Li alloys is T_1 [1], which was observed in both the FC and FC+HPT samples, see Fig. 7. The Orowan bypassing model has been utilized under the assumption that the precipitates are not shearable. Whether T_1 is truly shearable has been a subject of extensive debate [61,62]. In Al–Cu–Li alloys, T_1 precipitates are primarily considered non-shearable when their diameter exceeds 80 nm [63]. Theoretically, as T_1 plates grow larger, the energy needed for a dislocation to cut through them increases because a larger precipitate–matrix interface must be created. This makes it harder for dislocations to shear the precipitates, leading to a transition from shearing to bypassing behavior [64].

Zhu and Starke [28], through computer simulations under applied stress, examined the equilibrium configuration of dislocation interactions with randomly dispersed unshearable precipitates of finite size. These simulations led to a modified Orowan formula for the number of plate-like precipitates on Al (111) matrix planes:

$$\sigma_p = \left(\sqrt{f_p} + 0.7 f_p \sqrt{\frac{d_p}{t_p}} + 0.12 f_p^{3/2} \frac{d_p}{t_p} \right) M \frac{0.12 G b}{\sqrt{d_p t_p}} \left(\ln \frac{0.079 d_p}{b} \right). \tag{10}$$

where, d_p, t_p and f_p represent the diameter, thickness and volume fraction of the precipitates, respectively. The volume fraction and the size of the precipitates were obtained from SAXS data, see Section 3.3.

3.5. The combination of different strengthening mechanisms

The present approach provides valuable insight into the strength evolution of the complex TMP and SPD-processed alloy under both FC and FC+HPT conditions, highlighting the relative contributions of various strengthening mechanisms in Al–Cu–Li alloys. Table 2 summarizes

the parameter values used in Eq. (6) and subsequent equations, all of which are derived from the literature or from the analyses discussed earlier.

A strong correlation is observed between the projected and experimentally determined yield strength for both the FC and FC+HPT samples, as shown in Fig. 10. In the FC condition, the primary strengthening mechanisms are solid solution strengthening and precipitation strengthening. After HPT, however, the dominant contributors shift towards grain boundary strengthening, solid solution strengthening, and dislocation strengthening. The effect of solid solution strengthening remains constant, as HPT primarily induces grain refinement and cold plastic deformation, which increase strength in the FC+HPT sample through grain boundary and dislocation strengthening. Since the concentration of solute atoms dissolved in the Al matrix does not change, the solid solution strengthening remains unaffected. Additionally, precipitation hardening decreases slightly, from 132 MPa to 101 MPa, which can be attributed to the reduction in precipitate volume in the FC sample after HPT. Nevertheless, the precipitates were not completely dissolved, as both the FC and FC+HPT samples retained them, as shown in the XRD diffractogram (see Fig. 7).

This analysis provides clear evidence that nanoscale grain refinement, precipitate distribution, and increased dislocation density play a critical role in the significant strength enhancement observed after HPT in the Al–Cu–Li alloy.

4. Conclusions

Advanced characterization techniques, such as XRD, SEM, TEM, and SAXS, were used to analyze the evolution of precipitates, dislocations, and hardness in an Al–Cu–Li alloy processed by FC and subsequently HPT. These techniques provided a comprehensive understanding of the distribution, morphology, and strengthening mechanisms of the precipitates during processing. The key findings from each method are summarized below, demonstrating how different microstructural features contribute to the overall strengthening behavior:

(a) XRD analysis confirmed the formation of T_1, T_2, and δ precipitates after FC, which persisted even after HPT. However, peak broadening in the diffraction patterns indicated an increase in microstrain, directly correlating with an increase in dislocation density.
(b) SEM analysis revealed a fine-grained structure with an average grain size of 2.7 μm after FC. High-magnification micrographs confirmed the absence of pores, indicating effective consolidation.
(c) TEM analysis further examined grain refinement and dislocation structures. After HPT, the grain size was reduced to approximately 52 nm. High-resolution TEM images confirmed the formation of a high-density dislocation network, highlighting the intense plastic deformation induced by HPT.
(d) SAXS analysis provided insights into precipitate evolution under strain. The results indicated partial dissolution of precipitates as strain increased. High strain during HPT led to the fragmentation of larger precipitates into smaller ones, altering the precipitation kinetics and slightly reducing their strengthening contribution.
(e) Strengthening mechanisms varied between FC and FC+HPT samples. In the FC condition, the primary strengthening mechanisms were precipitation hardening and solid solution strengthening. However, after HPT, strength contributions shifted significantly, towards dislocation strengthening, solid solution strengthening, and grain boundary strengthening. These changes are attributed to microstructural refinement, increased dislocation density, and altered precipitation behavior induced by HPT.

These findings provide a deeper understanding of how HPT affects dislocation structures, precipitation behavior, and grain size evolution in the FC-processed alloy, ultimately influencing its enhanced mechanical properties.

CRediT authorship contribution statement

Elizabeth Mathew: Writing – original draft, Visualization, Validation, Methodology, Conceptualization. **Jürgen Markmann:** Writing – review & editing, Supervision, Conceptualization. **Chang Yin-Cheng Chan:** Writing – review & editing, Validation, Resources. **Yulia Ivanisenko:** Writing – review & editing, Validation, Resources. **Henry Ovri:** Writing – review & editing, Validation. **Uceu Fuad Hasan Suhuddin:** Writing – review & editing, Validation. **Peter Staron:** Writing – review & editing, Validation. **Benjamin Klusemann:** Writing – review & editing, Supervision, Funding acquisition, Conceptualization.

Funding

This project has received funding from the European Research Council (ERC) under the European Union's Horizon 2020 research and innovation programme (grant agreement No 101001567).

Declaration of competing interest

The authors declare that they have no known competing financial interests or personal relationships that could have appeared to influence the work reported in this paper.

Acknowledgment

The authors express sincere thanks to our colleague Annette Havelberg for her support in terms of language corrections.

Appendix A. SEM micrograph of Al–Cu–Li powder consolidated with only HPT

The SEM micrograph of Al–Cu–Li powder consolidated using HPT, taken at the edge where the strain is highest, is shown in Fig. 11 at its highest magnification. Following consolidation with HPT alone, holes ranging in size from 50 to 324 nm were observed in the sample.

Appendix B. XRD diffractogram

The XRD diffractograms in Fig. 12 show that the initial Al–Cu–Li alloy powder contains Al, Cu, Al_2Cu (θ' phase), and the δ phase as the primary constituents. After HPT processing, the formation of the T_2 becomes evident, particularly from the appearance of the characteristic diffraction peaks at $2\theta \approx 24°$ and 40°.

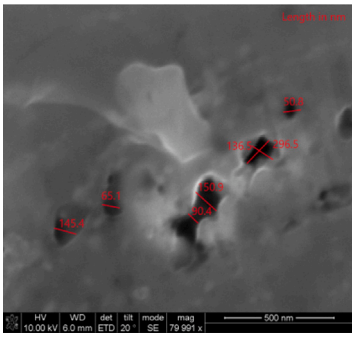

Fig. 11. SEM micrograph of Al–Cu–Li powder compacted with only HPT. The length of pores in nm is indicated in red.

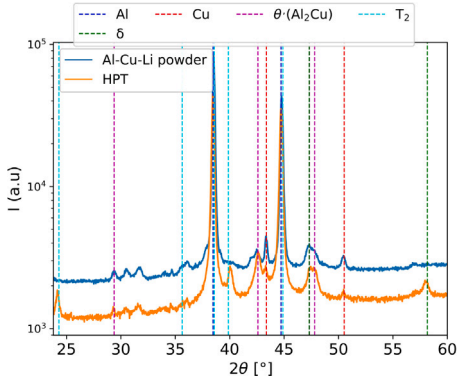

Fig. 12. XRD diffractograms of the initial Al–Cu–Li powder and the powder consolidated by HPT, showing phase evolution following deformation.

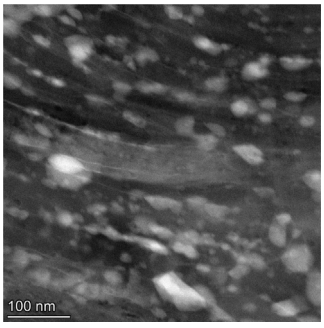

Fig. 13. STEM HAADF image of the HPT-consolidated Al–Cu–Li powder showing fragmented precipitates and coarse grain-boundary particles, along with a high dislocation density characteristic of severe plastic deformation.

Appendix C. STEM micrograph of Al–Cu–Li powder consolidated using only HPT

Fig. 13 shows a STEM micrograph of the Al–Cu–Li powder consolidated solely by HPT. Consistent with the XRD results in Fig. 12, the visible coarse precipitates are likely T_2 or δ phases. The micrograph reveals fragmented precipitates together with a high density of dislocations, both characteristic of severe plastic deformation. Spherical and irregularly shaped precipitates are observed along grain boundaries. According to previous studies [1,5], such grain-boundary precipitates are typically associated with T_2 or δ phases in Al–Cu–Li alloys, both of which tend to form as relatively coarse, incoherent or semi-coherent particles during deformation or low-temperature processing [5].

Appendix D. Phase diagram of Al–4.4 wt.% Cu-Li

Fig. 14 shows the calculated phase diagram for the Al–4.4 wt.% Cu–Li alloy generated using PanAluminium database in the PANDAT software [65,66]. The vertical dashed line marks a Li content of 1.6 wt.%, which corresponds to the alloy composition used in this study. Thermodynamic calculation indicates that at the HPT processing temperature of approximately 40 °C, the stable phases are T_2 and δ (B32), as highlighted by the red point. At the friction-consolidation (FC) processing temperature of approximately 500 °C, the T_1 phase becomes stable, as indicated by the green point.

Appendix E. Initial process parameter study for friction consolidation of Al–4.4 wt.% Cu–1.6 wt.% Li alloy

The microstructure of the initial parameter analysis carried out to determine appropriate friction consolidation (FC) settings for the

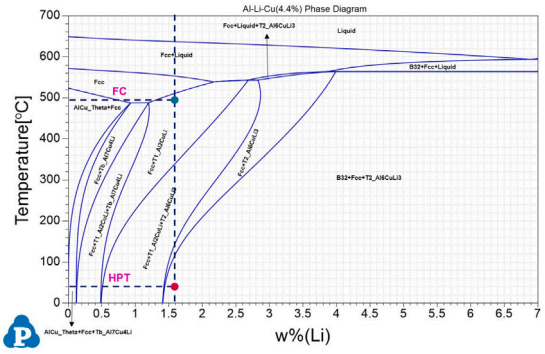

Fig. 14. Calculated phase diagram of Al–4.4 wt.% Cu–Li. The vertical dashed line marks the alloy composition (1.6 wt.% Li). The horizontal dashed lines correspond to the processing temperatures of HPT (≈40 °C) and FC (≈500 °C). The red point indicates the phases expected at the HPT temperature (T_2 and δ), while the green point marks the stable phase at the FC temperature (T_1).

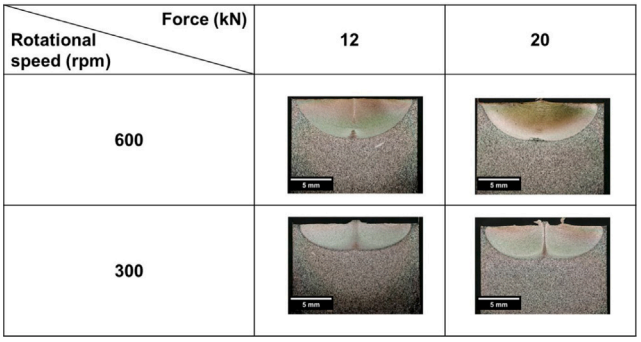

Fig. 15. Various consolidated regions in preliminary parameter study of friction consolidation on the investigated alloy.

examined alloy are displayed in Fig. 15. The consolidated regions and the transition to the surrounding, unconsolidated powder are clearly visible. At lower rpm, only partial consolidation was achieved. However, at an applied load of 12 kN and a rotation speed of 600 rpm, the material exhibited a well-consolidated microstructure with refined and equiaxed grains. This condition was subsequently selected for further processing within the presented study.

Data availability

The data obtained from this research is available on ZENODO (10.5281/zenodo.17847594).

References

[1] Thomas Dorin, Alireza Vahid, Justin Lamb, Aluminium lithium alloys, in: Fundamentals of Aluminium Metallurgy, Elsevier, 2018, pp. 387–438.
[2] N. Eswara Prasad, Amol Gokhale, Russell J.H. Wanhill, Aluminum-Lithium Alloys: Processing, Properties, and Applications, Butterworth-Heinemann, 2013.
[3] M.J. Starink, A. Deschamps, S.C. Wang, The strength of friction stir welded and friction stir processed aluminium alloys, Scr. Mater. 58 (5) (2008) 377–382.
[4] Chang Yin-Cheng Chan, Uceu FHR Suhuddin, Emad Maawad, Mark T Mordridge, Benjamin Klusemann, Precipitation distribution in mechanically alloyed Al-Cu-Li powders processed via friction consolidation, Mater. Des. (2025) 114847.
[5] N. Eswara Prasad, Amol A. Gokhale, R.J.H. Wanhill, Aluminium–lithium alloys, Aerosp. Mater. Mater. Technol.: Vol. 1: Aerosp. Mater. (2017) 53–72.
[6] Alexander P. Zhilyaev, Terence G. Langdon, Using high-pressure torsion for metal processing: Fundamentals and applications, Prog. Mater. Sci. 53 (6) (2008) 893–979.
[7] Ruslan Z. Valiev, Terence G. Langdon, Principles of equal-channel angular pressing as a processing tool for grain refinement, Prog. Mater. Sci. 51 (7) (2006) 881–981.

[8] Jenő Gubicza, I. Schiller, Nguyen Quang Chinh, J. Illy, Z. Horita, T.G. Langdon, The effect of severe plastic deformation on precipitation in supersaturated Al–Zn–Mg alloys, Mater. Sci. Eng.: A 460 (2007) 77–85.

[9] Pengcheng Ma, Takahiro Masuda, Shoichi Hirosawa, Zenji Horita, Development of high-strength Al–Cu–Mg alloy by combined application of high-pressure torsion and aging treatment, Mater. Trans. 64 (2) (2023) 514–521.

[10] Ying Chen, Xu Yuan, Jiahui Dong, Shenbao Jin, Gang Sha, Yihang Yang, Houan Zhang, Chuanting Wang, Nong Gao, Marco J. Starink, The nanoscale mechanisms of strengthening and ductility enhancement in an Al–Mg–Si–Mn alloy on processing by high-pressure torsion, Mater. Charact. 203 (2023) 113145.

[11] Jiahui Dong, Nong Gao, Ying Chen, Lingfei Cao, Hui Song, Hannes Fröck, Benjamin Milkereit, Marco J. Starink, Achieving ultra-high strength of Al-Cu-Li alloys by the combination of high pressure torsion and age-hardening, Mater. Sci. Eng.: A 832 (2022) 142504.

[12] Michael Vyacheslavovich Markushev, Elena Viktorovna Avtokratova, Stanislav Vatslavovich Krymskiy, Vyacheslav Vladimirovich Tereshkin, Oleg Shamilevich Sitdikov, Effect of HPT straining and further natural aging on the structure and hardness of aluminum alloy 1965 with nanosized TM aluminides, Lett. Mater. 12 (4s) (2022) 463–468.

[13] A. Matsumuro, K. Sakai, M. Senoo, High-pressure phase diagram of an aluminium-rich Al-Li alloy at a pressure of 5.4 GPa, J. Mater. Sci. 28 (24) (1993) 6567–6570.

[14] Elizabeth Mathew, Rupesh Chafle, Benjamin Klusemann, CALPHAD-based modeling of pressure-dependent Al, Cu and Li unary systems, Calphad 85 (2024) 102692.

[15] Shuaishuai Qin, Seungwon Lee, Taiki Tsuchiya, Kenji Matsuda, Zenji Horita, Robert Kocisko, Tibor Kvackaj, Aging behavior of Al-Li-(Cu, Mg) alloys processed by different deformation methods, Mater. Des. 196 (2020) 109139.

[16] Nicole R. Overman, Matthew J. Olszta, M. Bowden, Xiao Li, Aashish Rohatgi, Suveen N. Mathaudhu, Glenn J. Grant, Scott A. Whalen, The onset of alloying in Cu-Ni powders under high-shear consolidation, Mater. Des. 211 (2021) 110151.

[17] David Catalini, Djamel Kaoumi, Anthony P. Reynolds, Glenn J. Grant, Friction Consolidation of MA956 powder, J. Nucl. Mater. 442 (1–3) (2013) S112–S118.

[18] Xiao Li, Dario Baffari, A.P. Reynolds, Friction stir consolidation of aluminum machining chips, Int. J. Adv. Manuf. Technol. 94 (2018) 2031–2042.

[19] Ahmed S.J. Al-Zubaydi, Nong Gao, Jan Dzugan, Pavel Podany, Sandeep Sahu, Deepak Kumar, Ying Chen, Philippa A.S. Reed, The hot deformation behaviour of laser powder bed fusion deposited Al–Si–Cu alloy processed by high-pressure torsion, J. Mater. Sci. 57 (43) (2022) 20402–20418.

[20] V.V. Stolyarov, Y.T. Zhu, T.C. Lowe, R.K. Islamgaliev, R.Z. Valiev, A two step SPD processing of ultrafine-grained titanium, Nanostruct. Mater. 11 (7) (1999) 947–954.

[21] Ahmed S.J. Al-Zubaydi, Nong Gao, Jan Džugan, Pavel Podanỳ, Ying Chen, Philippa A.S. Reed, Fracture behaviour assessment of the additively manufactured and HPT-processed Al–Si–Cu alloy, Mater. Sci. Technol. 41 (8) (2025) 592–613.

[22] Jorge F. Dos Santos, Peter Staron, Torben Fischer, Joseph D. Robson, Aleksander Kostka, P. Colegrove, Hua Wang, Jakob Hilgert, L. Bergmann, Leon Leander Hütsch, et al., Understanding precipitate evolution during friction stir welding of Al-Zn-Mg-Cu alloy through in-situ measurement coupled with simulation, Acta Mater. 148 (2018) 163–172.

[23] Xiao Li, Study of Friction Extrusion and Consolidation (Ph.D. thesis), University of South Carolina, 2016.

[24] Amandine Duchaussoy, Xavier Sauvage, Alexis Deschamps, Frederic De Geuser, Gilles Renou, Zenji Horita, Complex interactions between precipitation, grain growth and recrystallization in a severely deformed Al-Zn-Mg-Cu alloy and consequences on the mechanical behavior, Materialia 15 (2021) 101028.

[25] Kaveh Edalati, Zenji Horita, A review on high-pressure torsion (HPT) from 1935 to 1988, Mater. Sci. Eng.: A 652 (2016) 325–352.

[26] Kaveh Edalati, Yoshihiko Yokoyama, Zenji Horita, High-pressure torsion of machining chips and bulk discs of amorphous Zr50Cu30Al10Ni10, Mater. Trans. 51 (1) (2010) 23–26.

[27] R.W. Fonda, J.F. Bingert, Precipitation and grain refinement in a 2195 Al friction stir weld, Met. Mater. Trans. A 37 (2006) 3593–3604.

[28] A.W. Zhu, E.A. Starke, Jr., Strengthening effect of unshearable particles of finite size: a computer experimental study, Acta Mater. 47 (11) (1999) 3263–3269.

[29] Zhixiong Zhu, Jian Han, Chong Gao, Mao Liu, Jianwei Song, Zhiwei Wang, Huijun Li, Microstructures and mechanical properties of Al-Li 2198-T8 alloys processed by two different severe plastic deformation methods: A comparative study, Mater. Sci. Eng.: A 681 (2017) 65–73.

[30] M. Murayama, Zenji Horita, K. Hono, Microstructure of two-phase Al–1.7 at.% Cu alloy deformed by equal-channel angular pressing, Acta Mater. 49 (1) (2001) 21–29.

[31] Olavo C. Haase, Paulo R. Cetlin, Roberto B. Figueiredo, Terence G. Langdon, Pedro Henrique R. Pereira, Tailoring a high-strength Al–4Cu alloy through processing of powders by up to 100 turns of high-pressure torsion, Mater. Sci. Eng.: A 882 (2023) 145454.

[32] Ricardo M. Halak, Lars Rath, Uceu F.H.R. Suhuddin, Jorge F. dos Santos, Benjamin Klusemann, Changes in processing characteristics and microstructural evolution during frictiousion of aluminum, Int. J. Mater. Form. 15 (3) (2022) 24.

[33] S. Van Smaalen, A. Meetsma, J.L. De Boer, P.M. Bronsveld, Refinement of the crystal structure of hexagonal Al2CuLi, J. Solid State Chem. 85 (2) (1990) 293–298.

[34] Christian Dwyer, Matthew Weyland, Lan-Yun Chang, B.C. Muddle, Combined electron beam imaging and ab initio modeling of T1 precipitates in Al–Li–Cu alloys, Appl. Phys. Lett. 98 (20) (2011).

[35] Ni Yu, Richard Portier, Denis Gratias, K. Yu-zhang, Jean-Yves Bigot, Al6CuLi3-T2: A Stable Icosahedral Phase?, Mater. Sci. Forum 22–24 (1987) 579–590.

[36] T. Ungár, A. Borbély, The effect of dislocation contrast on x-ray line broadening: A new approach to line profile analysis, Appl. Phys. Lett. 69 (21) (1996) 3173–3175.

[37] J. Markmann, V. Yamakov, J. Weissmüller, Validating grain size analysis from X-ray line broadening: a virtual experiment, Scr. Mater. 59 (1) (2008) 15–18.

[38] G.K. Williamson, R.E. Smallman, III, Dislocation densities in some annealed and cold-worked metals from measurements on the X-ray debye-scherrer spectrum, Phil Mg, Cilt 1 (1956) 134-134.

[39] David B. Williams, C. Barry Carter, The transmission electron microscope, in: Transmission Electron Microscopy: A Textbook for Materials Science, Springer, 1996, pp. 3–17.

[40] Seungwon Lee, Zenji Horita, Shoichi Hirosawa, Kenji Matsuda, Age-hardening of an Al–Li–Cu–Mg alloy (2091) processed by high-pressure torsion, Mater. Sci. Eng.: A 546 (2012) 82–89.

[41] R. Vafaei, M.R. Toroghinejad, R. Pippan, Evaluation of mechanical behavior of nano-grained 2024 Al alloy during high pressure torsion (HPT) process at various temperatures, Mater. Sci. Eng.: A 536 (2012) 73–81.

[42] M.H. Hong, K. Hono, W.T. Reynolds, T. Tarui, Atom probe and transmission electron microscopy investigations of heavily drawn pearlitic steel wire, Met. Mater. Trans. A 30 (1999) 717–727.

[43] Jianhua Jiang, Yi Ding, Fangqing Zuo, Aidang Shan, Mechanical properties and microstructures of ultrafine-grained pure aluminum by asymmetric rolling, Scr. Mater. 60 (10) (2009) 905–908.

[44] Takaaki Tanaka, Yuki Toji, Paweł Kozikowski, Masato Ohnuma, Miho Nagano, SAXS and TEM quantitative analysis of plate-like precipitates in Ti-added low-carbon steel, ISIJ Int. 60 (10) (2020) 2246–2254.

[45] K. Satya Prasad, A.K. Mukhopadhyay, A.A. Gokhale, D. Banerjee, D.B. Goel, [delta] precipitation in an Al-Li-Cu-Mg-Zr alloy, Scr. Met. Materialia;(United States) 30 (10) (1994).

[46] W.T. Sun, X.G. Qiao, M.Y. Zheng, Y. He, Nan Hu, C. Xu, N. Gao, M.J. Starink, Exceptional grain refinement in a Mg alloy during high pressure torsion due to rare earth containing nanosized precipitates, Mater. Sci. Eng.: A 728 (2018) 115–123.

[47] M.J. Starink, A. Cerezo, J.L. Yan, N. Gao, Reply to the comments on "Room-temperature precipitation in quenched Al–Cu–Mg alloys: a model for the reaction kinetics and yield-strength development", Phil. Mag. Lett. 86 (04) (2006) 243–252.

[48] M.J. Starink, S.C. Wang, The thermodynamics of and strengthening due to co-clusters: general theory and application to the case of Al–Cu–Mg alloys, Acta Mater. 57 (8) (2009) 2376–2389.

[49] Jiu Wen Zhang, Marco J. Starink, Nong Gao, Wen Long Zhou, Influence of strain reversals during high pressure torsion process on strengthening in Al-Cu-Mg (-Li) alloy, in: Materials Science Forum, vol. 667, Trans Tech Publ, 2011, pp. 809–814.

[50] M. Tiryakioğlu, On the relationship between vickers hardness and yield stress in Al–Zn–Mg–Cu alloys, Mater. Sci. Eng.: A 633 (2015) 17–19.

[51] Peng Zhang, S.X. Li, Z.F. Zhang, General relationship between strength and hardness, Mater. Sci. Eng.: A 529 (2011) 62–73.

[52] Ying Chen, Nong Gao, Gang Sha, Simon P. Ringer, Marco J. Starink, Microstructural evolution, strengthening and thermal stability of an ultrafine-grained Al–Cu–Mg alloy, Acta Mater. 109 (2016) 202–212.

[53] O.R. Myhr, Ø. Grong, H.G. Fjær, C.D. Marioara, Modelling of the microstructure and strength evolution in Al–Mg–Si alloys during multistage thermal processing, Acta Mater. 52 (17) (2004) 4997–5008.

[54] Jiuwen Zhang, Nong Gao, Marco J. Starink, Al–Mg–Cu based alloys and pure Al processed by high pressure torsion: The influence of alloying additions on strengthening, Mater. Sci. Eng.: A 527 (15) (2010) 3472–3479.

[55] Jan Herrnring, Peter Staron, Nikolai Kashaev, Benjamin Klusemann, Multiscale process simulation of residual stress fields of laser beam welded precipitation hardened AA6082, Materialia 3 (2018) 243–255.

[56] Rosen Ivanov, Alexis Deschamps, Frédéric De Geuser, Clustering kinetics during natural ageing of Al-Cu based alloys with (Mg, Li) additions, Acta Mater. 157 (2018) 186–195.

[57] Megumi Kawasaki, Roberto B. Figueiredo, Terence G. Langdon, An investigation of hardness homogeneity throughout disks processed by high-pressure torsion, Acta Mater. 59 (1) (2011) 308–316.

[58] Niels Hansen, Hall–Petch relation and boundary strengthening, Scr. Mater. 51 (8) (2004) 801–806.

[59] T. Shanmugasundaram, M. Heilmaier, B.S. Murty, V. Subramanya Sarma, On the Hall–Petch relationship in a nanostructured Al–Cu alloy, Mater. Sci. Eng.: A 527 (29–30) (2010) 7821–7825.

[60] Takahiro Masuda, Xavier Sauvage, Shoichi Hirosawa, Zenji Horita, Achieving highly strengthened Al–Cu–Mg alloy by grain refinement and grain boundary segregation, Mater. Sci. Eng.: A 793 (2020) 139668.
[61] Thomas Dorin, Alexis Deschamps, Frédéric De Geuser, Christophe Sigli, Quantification and modelling of the microstructure/strength relationship by tailoring the morphological parameters of the T1 phase in an Al–Cu–Li alloy, Acta Mater. 75 (2014) 134–146.
[62] Thomas Dorin, Frédéric De Geuser, Williams Lefebvre, Christophe Sigli, Alexis Deschamps, Strengthening mechanisms of T1 precipitates and their influence on the plasticity of an Al–Cu–Li alloy, Mater. Sci. Eng.: A 605 (2014) 119–126.
[63] Xiao-Ming Wang, Wen-Zhu Shao, Jian-Tang Jiang, Guo-Ai Li, Xiao-Ya Wang, Liang Zhen, Quantitative analysis of the influences of pre-treatments on the microstructure evolution and mechanical properties during artificial ageing of an Al–Cu–Li–Mg–Ag alloy, Mater. Sci. Eng.: A 782 (2020) 139253.
[64] Yong Yang, Guoai He, Yu Liu, Kai Li, Wenke Wu, Cheng Huang, Quantitative contribution of T1 phase to the strength of Al-Cu-Li alloys, J. Mater. Sci. 56 (33) (2021) 18368–18390.
[65] CompuTherm LLC, Introducing pandat software - an integrated modeling platform for materials design, 2025, https://computherm.com/. (Acessed 10 November 2025).
[66] Weisheng Cao, S.-L. Chen, Fan Zhang, K. Wu, Y. Yang, Y.A. Chang, R. Schmid-Fetzer, W.A. Oates, PANDAT software with PanEngine, PanOptimizer and PanPrecipitation for multi-component phase diagram calculation and materials property simulation, Calphad 33 (2) (2009) 328–342.